

The thermomagnetic instability in superconducting films with adjacent metal layer

J. I. Vestgård, ¹ Y. M. Galperin, ^{1,2} and T. H. Johansen^{1,3}

¹*Department of Physics, University of Oslo, P. O. box 1048 Blindern, 0316 Oslo, Norway*

²*Ioffe Physical Technical Institute, 26 Polytekhnicheskaya, St Petersburg 194021, Russian Federation*

³*Institute for Superconducting and Electronic Materials,
University of Wollongong, Northfields Avenue, Wollongong, NSW 2522, Australia*

Dendritic flux avalanches is a frequently encountered consequence of the thermomagnetic instability in type-II superconducting films. The avalanches, potentially harmful for superconductor-based devices, can be suppressed by an adjacent normal metal layer, even when the two layers are not in thermal contact. The suppression of the avalanches in this case is due to so-called magnetic braking, caused by eddy currents generated in the metal layer by propagating magnetic flux. We develop a theory of magnetic braking by analyzing coupled electrodynamics and heat flow in a superconductor-normal metal bilayer. The equations are solved by linearization and by numerical simulation of the avalanche dynamics. We find that in an uncoated superconductor, even a uniform thermomagnetic instability can develop into a dendritic flux avalanche. The mechanism is that a small non-uniformity caused by the electromagnetic non-locality induces a flux-flow hot spot at a random position. The hot spot quickly develops into a finger, which at high speeds penetrates into the superconductor, forming a branching structure. Magnetic braking slows the avalanches, and if the normal metal conductivity is sufficiently high, it can suppress the formation of the dendritic structure. During avalanches, the braking by the normal metal layer prevents the temperature from exceeding the transition temperature of the superconductor. Analytical criteria for the instability threshold are developed using the linear stability analysis. The criteria are found to match quantitatively the instability onsets obtained in simulation.

PACS numbers: 74.25.Ha, 68.60.Dv, 74.78.-w

I. INTRODUCTION

The concept of the critical state introduced by Bean¹ is widely used to describe various physical properties in the vortex phase of type-II superconductors, see, e.g., Refs. 2 and 3, and references therein. According to Bean, the driving force of the currents is balanced by the pinning force from material inhomogeneities, with a strength characterized by the critical current density, j_c . The dissipation becomes vanishing if the current density j is less than j_c .

However, the critical state can be unstable with respect to fluctuations, e.g., in the temperature. Since j_c decreases with increasing temperature, a fluctuation causing an increase of the temperature will facilitate further penetration of magnetic flux into the sample, and consequently more dissipation. This positive feedback loop is the mechanism behind the thermomagnetic instability,^{4,5} see also Refs. 6 and 7 for a review. In bulk samples the instability often results in large flux jumps, sometimes causing the entire superconductor to heat above its superconducting transition temperature, T_c .⁸ In thin films, the instability leads to flux avalanches showing complex dendritic structures.^{9–11} In both cases the system is bistable since it, after some time, reaches a stable highly dissipative state characterized by linear response of the current to electric field.¹² Criteria for onset of the thermomagnetic instability were first considered for bulks under adiabatic conditions.^{4,5,13} The theory was later extended to include also the flow of heat,^{14–17} and it was found that the instability onset can

be accompanied by oscillations in temperature.^{18,19} For superconducting films in transverse geometry, the analysis is complicated by the fact that the electrodynamics is nonlocal.^{20,21} Also, close to the critical state, the response of the electric field to fluctuations in the current density is strongly nonlinear.^{22,23} Therefore, one has to address an essentially nonlocal and nonlinear dynamical problem. Nevertheless, linear stability analysis has succeeded in providing criteria for the lower threshold field for onset of the instability and the upper threshold temperature, which may be significantly lower than T_c .^{24–26} It has also been shown that edge defects can lower the threshold for onset of the instability.^{27,28} The time evolution of dendritic flux avalanches has been investigated using numerical simulations, which produce patterns in striking resemblance with experiments.^{25,26,29–32}

To prevent the thermomagnetic instability to occur, superconducting cables are constructed by embedding superconducting filaments in a normal-metal matrix.³³ Indeed, experiments also show that a metallic layer is beneficial for the stability of superconducting films, as it can completely suppress dendritic flux avalanches.^{34,35} The suppression becomes more efficient as the thickness of the metallic layer increases.^{36,37} It has also been reported that avalanches change direction when meeting the metal-covered part of a superconducting sample.^{38–40} The proposed mechanism behind the observed suppression was based on the idea that the normal-metal layer acts as a thermal shunt, decreasing temperature gradients.³⁴ However, experiments have demonstrated that the avalanche activity can be reduced even when there is a spatial gap between the metal and

the superconductor.⁴¹ This shows that avalanches can be prevented also by the eddy currents induced in the metal, i.e., a magnetic braking effect. Further evidences of the avalanche-induced non-stationary eddy currents in an adjacent metal layer, are the voltage pulses appearing when branches of dendritic flux avalanches take place under the metal layer in a partly metal-covered superconducting film.⁴²

In the present work we will investigate the stability of the flux distributions in a superconducting film located close to a normal-metal layer. The analysis focuses on the process of magnetic braking, so we will assume that there is no thermal contact between the two layers. Magnetic braking is a dynamic effect, so in order to understand how it operates it is necessary to compare the time evolutions of metal-covered and pristine superconductors. Hence, a large portion of the present work is devoted to the study of pristine superconductors.

To reach our goal we will use a combination of linear stability analysis and numerical simulations. The linear stability analysis will provide the conditions for onset of instability, while the simulations allow us to follow the full time evolution, from nucleation of the instability to the formation of the dendritic structures. The analysis is repeated with a metal layer included, but under otherwise identical conditions. We will thus find how the magnetic braking affects dendritic flux avalanches.

In the study of the pristine superconductors, we will pay particular attention to the long wavelength modes of the Fourier space linear stability analysis. Such modes are particularly interesting because they become unstable at low electric field, but they have been neglected in previous linear stability analysis focused on nucleation of finger-like patterns elongated transverse to the edge. A major question addressed in the present work is if a uniform thermomagnetic instability can develop into a dendritic structure.

The paper is organized as follows. Section II describes the model and outlines the setup for simulations. Section III finds a formal solution of the equations to first order in the perturbations. Section IV considers the stability of uncoated superconductors. Section V considers the stability of metal-coated superconductors. Section VI gives the summary and discussion.

II. MODEL

A. Basic Equations

Let us consider a superconducting strip with an adjacent metal layer, as depicted in Fig. 1. For simplicity we assume that there is no thermal coupling between the superconductor and the normal metal, while the superconductor is thermally coupled to the substrate, which is kept at constant temperature T_0 . The thickness of the metal, d_m , and superconductor, d_s , are both much smaller than the strip width, $2w$. Therefore, we can

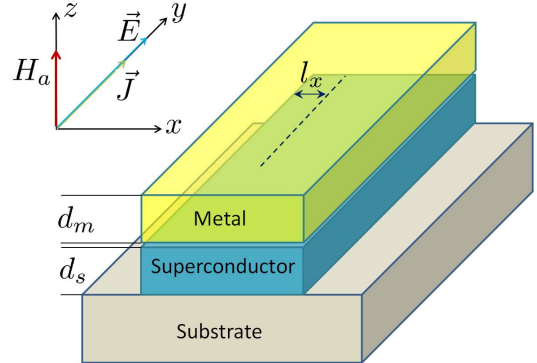


FIG. 1. (color online) Sketch of the system: a thin superconducting strip of thickness d_s with a deposited metal layer of thickness d_m . The superconductor is in thermal contact with the substrate, kept at constant temperature T_0 , but not with the metal. Current flows in the y direction and flux has penetrated a distance l_x from both sides due to the applied magnetic field H_a .

parametrize the problem using the sheet current \mathbf{J} , defined as $\mathbf{j} = \mathbf{J}\delta(z)$, where \mathbf{j} is the total current density and $\delta(z)$ is the Dirac delta function.

The sheet current \mathbf{J} entering the Maxwell equations consists of two contributions,¹²

$$\mathbf{J} = \mathbf{J}_s + \mathbf{J}_m, \quad (1)$$

where and \mathbf{J}_s and \mathbf{J}_m are the sheet currents in the superconductor and metal layer, respectively. Since the two layers are close, the electric field, \mathbf{E} , is approximately the same in the two layers, giving

$$\mathbf{J}_s = d_s \sigma_s \mathbf{E}, \quad \mathbf{J}_m = d_m \sigma_m \mathbf{E}. \quad (2)$$

The conductivity of the metal, σ_m , is assumed to be E -independent. The current-voltage relation in the superconducting film is assumed to be non-Ohmic with E -dependent conductance expressed as^{22,23}

$$\sigma_s = \frac{1}{\rho_n} \begin{cases} (Ed_s/\rho_n J_c)^{1/n_s-1}, & J < J_c \text{ and } T < T_c, \\ 1, & \text{otherwise.} \end{cases} \quad (3)$$

Here T is the local temperature, $J_c = dj_c$ is the sheet critical current, ρ_n is the resistivity of the superconductor in the normal state, and n_s is the creep exponent.

The electrodynamics is governed by the Maxwell equations,

$$\nabla \times \mathbf{E} = -\dot{\mathbf{B}}, \quad \nabla \cdot \mathbf{B} = 0, \quad \nabla \times \mathbf{H} = \mathbf{J}\delta(z), \quad (4)$$

with $\mathbf{B} = \mu_0 \mathbf{H}$ and $\nabla \cdot \mathbf{J} = 0$. The flow of heat in the superconductor is described by the energy balance equation describing the interplay between Joule heating, thermal conduction along the film, and heat transfer to the substrate. It reads as

$$c\dot{T} = \kappa \nabla^2 T - \frac{h}{d_s} (T - T_0) + \frac{1}{d_s} \mathbf{J}_s \cdot \mathbf{E}, \quad (5)$$

with superconductor specific heat c , heat conductivity κ , coefficient of heat transfer to substrate h . Since there is no thermal contact between the metal and the superconductor there is no need to calculate the flow of heat in the normal metal.

B. Dimensionless form

For further analysis it is convenient to express the equations in a dimensionless form. We denote

$$\tilde{T} = \frac{T}{T_c}, \quad \tilde{J} = \frac{J}{J_{c0}}, \quad \tilde{J}_c = \frac{J_c}{J_{c0}}, \quad \tilde{H} = \frac{H}{J_{c0}}, \quad \tilde{x} = \frac{x}{w}, \quad \tilde{y} = \frac{y}{w}, \\ \tilde{t} = t \frac{\rho_n}{\mu_0 d_s w}, \quad \tilde{E} = \frac{E}{\rho_n j_{c0}}, \quad \tilde{\sigma}_s = \sigma_s \rho_n, \quad \tilde{\sigma}_m = \sigma_m \rho_n \frac{d_m}{d_s}.$$

Here J_{c0} is the sheet critical current at $T = 0$. Henceforth we omit the tildes for brevity. In these units the heat propagation equation reads as

$$\dot{T} = \alpha \nabla^2 T - \beta(T - T_0) + \gamma \bar{\gamma} J_s E, \quad (6)$$

where $\bar{\gamma} = c(T_c)/c(T)$ is a function of temperature and α , β , and γ are constants, provided the ratios κ/c and h/c are independent of temperature (that we assume). In Eq. (6), α is dimensionless heat conductivity, β is dimensionless constant for heat transfer to the substrate, and γ is the Joule heating parameter. The dimensionless material parameters are related to the physical parameters as

$$\alpha = \frac{\mu_0 \kappa d}{\rho_n c w}, \quad \beta = \frac{\mu_0 w h}{\rho_n c}, \quad \gamma = \frac{\mu_0 w d j_{c0}^2}{T_c c}, \quad (7)$$

where all quantities are evaluated at T_c .

The dimensionless Maxwell equations are

$$\nabla \times \mathbf{E} = -\dot{\mathbf{H}}, \quad \nabla \cdot \mathbf{H} = 0, \quad \nabla \times \mathbf{H} = \mathbf{J} \delta(z). \quad (8)$$

The material laws can be expressed in the dimensionless form as

$$J_s = \begin{cases} J_c (E/J_c)^{1/n_s}, & J < J_c \text{ and } T < 1, \\ E, & \text{otherwise,} \end{cases} \\ J_m = \sigma_m E. \quad (9)$$

The above expressions are valid for arbitrary temperature dependencies of J_c , n_s and $\bar{\gamma}$. To be specific, we will assume cubic temperature dependencies for κ , h , and c , and linear temperature dependency for J_c , as typical for low- T_c superconductors and MgB₂, i.e.,

$$J_c = 1 - T, \quad n_s = n_1/T, \quad \bar{\gamma} = T^{-3}. \quad (10)$$

The parameters used in the calculations of this work are chosen to be compatible with the formation of dendritic structures. For example, we let $\alpha = 10^{-5}$, $\beta = 0.1$, $\gamma = 10$, and $n_1 = 20$.³¹ In our analysis, the electric field is kept as a free variable. However, one should keep in mind that in the critical state it is proportional to

the ramp rate of the applied magnetic field, $E \sim \dot{H}_a$.⁴³ This relationship is needed to bring together the linear stability analysis with numerical simulations and experiment. In most experiments the ramp rate is moderate, say $\dot{H}_a \ll 10^{-4}$.

C. Numerical procedure

The simulations are performed for an infinitely long strip extended in the y direction, as depicted in Fig. 1. We analyze the full nonlinear problem by numerical time integration of Eq. (6) (the heat flow equation) and Eq. (8) (the Maxwell equations) with the material relations given by Eq. (9) and temperature dependencies given by Eq. (10). The set of boundary conditions and the calculation procedure are detailed in Ref. 29.

In order to make the comparison with the linearized theory as close as possible and elucidate dynamics of the dendrites, the numerical analysis is conducted in two separate steps.

At the first step we find the background flux distribution by solving the Maxwell equations decoupled from the thermal effects. For that we put $\gamma = 0$, starting from a zero-field-cooled state, and ramp applied magnetic field with a constant rate \dot{H}_a until the flux has penetrated over a given distance l_x .

At the second step the thermal feedback is turned on by putting $\gamma > 0$. The state will then start evolving, and the difference from the background state is called the perturbation. The background state is stable if the perturbation saturates to some small value and unstable if it develops into a dendritic flux avalanche.

It is worth noting that the formulated numerical procedure differs from the conventional linear stability analysis in several aspects. In particular, (i) the perturbations (as they are defined above) are not necessarily small; (ii) the background distributions of B_z , \mathbf{E} , \mathbf{J} , and T are essentially non-uniform; (iii) The electromagnetic boundary conditions are more proper; (iv) due to flux creep, the maximum current density in the critical state is slightly lower than the critical current density, i.e., $J \sim J_c (\dot{H}_a/J_c)^{1/n_s}$.

The numerical procedure of this work deviates from previous numerical simulations of dendritic flux avalanches in the absence of randomly distributed disorder. Such disorder is important since it causes fluctuations in the background E -values, which may trigger avalanches.^{29,30} However, for simplicity of the calculations and the analysis, the present work considers only spatially uniform samples.

III. LINEAR STABILITY ANALYSIS

Let us assume that we start from a uniform background distributions of the electric field $\mathbf{E} \equiv E \hat{\mathbf{y}}$ and temperature T , as depicted in Fig. 1. Due to the applied magnetic

field or current, the magnetic flux front, and thus also the fronts of E and T have reached a distance l_x from both edges. The perturbed values of \mathbf{E} and T are specified as $\mathbf{E} + \delta\mathbf{E}$ and $T + \delta T$. To meet the boundary conditions we assume that in the Fourier space the perturbations are of the form

$$\begin{aligned}\delta E_x &= \varepsilon_x e^{\lambda t} \sin(k_x x) \sin(k_y y), \\ \delta E_y &= \varepsilon_y e^{\lambda t} \cos(k_x x) \cos(k_y y), \\ \delta T &= \theta e^{\lambda t} \cos(k_x x) \cos(k_y y),\end{aligned}\quad (11)$$

where k_x and k_y are the in-plane wavevectors and λ is the instability increment. The flux penetration depth sets the lower limit for allowed wave-vectors in x direction and we will thus identify $l_x = \pi/2k_x$. The electrical current and magnetic field perturbations are

$$\begin{aligned}\delta J_x &= i_x e^{\lambda t} \sin(k_x x) \sin(k_y y), \\ \delta J_y &= i_y e^{\lambda t} \cos(k_x x) \cos(k_y y), \\ \delta H_z &= b e^{\lambda t} \sin(k_x x) \cos(k_y y).\end{aligned}\quad (12)$$

We will now linearize the equations in the perturbations and find a solution for the instability increment $\lambda = \lambda(E, T, k_x, k_y)$.

After linearizing the product $J_s E$ in Eq. (6) and making Fourier transform we express the heat propagation equation as

$$\left[\lambda + \alpha k^2 + \beta + \frac{n_s - 1}{n_s} \frac{\gamma \bar{\gamma} J_s E}{T^*} \right] \theta = \frac{n_s + 1}{n_s} \gamma \bar{\gamma} J_s \varepsilon_y, \quad (13)$$

where $1/T^* \equiv |\partial \ln J_c / \partial T|$ and $k = \sqrt{k_x^2 + k_y^2}$. We have used that $\delta|\mathbf{E}| = \delta E_y$ due to the boundary condition $\mathbf{E} \cdot \hat{\mathbf{x}} = 0$. The temperature derivative of $\bar{\gamma}$ has been ignored.

The perturbations of the current components i_x and i_y are related to ε and θ through Eq. (9) (the material laws), which gives for the Fourier amplitudes of the perturbations

$$i_x = \frac{J}{E} \varepsilon_x, \quad i_y = \frac{J}{nE} \varepsilon_y - \frac{n_s - 1}{n_s} \frac{J_s}{T^*} \theta. \quad (14)$$

Here we have introduced the nonlinearity exponent of the composite system, $n = n(E, T)$, as

$$n \equiv \frac{\partial \ln E}{\partial \ln J} = n_s \frac{1 + J_m/J_s}{1 + n_s J_m/J_s}. \quad (15)$$

When electric field is small most current flows in the superconductor, giving $n \approx n_s$. For high electric fields, the current may flow in the normal metal and this is the regime in which we expect that magnetic braking can suppress the thermomagnetic instability.

The value of ε_x is fixed by requiring continuity of the current, $\nabla \cdot \delta\mathbf{J} = 0$, giving $k_x i_x - k_y i_y = 0$. Thus

$$\varepsilon_x = \frac{E}{J} \frac{k_y}{k_x} i_y = \frac{k_y}{k_x} \left[\frac{1}{n} \varepsilon_y - \frac{n_s - 1}{n_s} \frac{E J_s}{J T^*} \theta \right]. \quad (16)$$

Using the Faraday law

$$\lambda b = k_x \varepsilon_y + k_y \varepsilon_x \quad (17)$$

and Eq. (16), we get

$$\lambda b = \frac{1}{k_x} \left(k_x^2 + \frac{k_y^2}{n} \right) \varepsilon_y - \frac{k_y^2}{k_x} \frac{n_s - 1}{n_s} \frac{E J_s}{J T^*} \theta. \quad (18)$$

The Biot-Savart law relates B_z with \mathbf{J} . Treating the film as infinite gives the simple relation⁴⁴

$$b = -\frac{1}{2} \frac{k}{k_x} i_y, \quad (19)$$

where the continuity of current has been used to eliminate i_x . The exact treatment of the film boundary would transform the above relation to a sum over k' , where the off-diagonal elements with $k' \neq k$ are largest for the longest wavelengths.⁴³ However, for the linear stability of the system, the diagonal elements are by far the most important, and we will keep only those in the stability estimates. Using the expression for the current, Eq. (14), we get

$$b = -\frac{k}{2} \frac{1}{k_x} \frac{J}{nE} \varepsilon_y + \frac{k}{2} \frac{1}{k_x} \frac{n_s - 1}{n_s} \frac{J_s}{T^*} \theta. \quad (20)$$

Combining Eqs. (18) and (20) we eliminate b , and after some algebra we get

$$\left[k_x^2 + \frac{k_y^2}{n} + \frac{k}{2} \frac{J}{nE} \lambda \right] \varepsilon_y = \frac{n_s - 1}{n_s} \frac{J_s}{T^*} \left[k_y^2 \frac{E}{J} + \frac{k}{2} \lambda \right] \theta.$$

Combining the above equation following from electrodynamics with Eq. (13), describing the heat flow, gives a quadratic eigenvalue equation for λ ,

$$A\lambda^2 + B\lambda + C = 0, \quad (21)$$

where

$$\begin{aligned}A &= \frac{k}{2} \frac{J}{nE}, \\ B &= k_x^2 + \frac{k_y^2}{n} + \frac{k}{2} \frac{\alpha k^2 + \beta}{nE} J - \frac{k}{2} \left(\frac{n_s + 1}{n_s} \frac{J_s}{J} - \frac{1}{n} \right) \frac{J_s}{J_c} J F, \\ C &= (\alpha k^2 + \beta) \left(k_x^2 + \frac{k_y^2}{n} \right) \\ &\quad + \left[k_x^2 - k_y^2 \left(\frac{n_s + 1}{n_s} \frac{J_s}{J} - \frac{1}{n} \right) \right] \frac{J_s}{J_c} E F, \\ F &\equiv \frac{n_s - 1}{n_s} \frac{\gamma \bar{\gamma} J_c}{T^*}.\end{aligned}\quad (22)$$

According to the temperature dependencies (10), $F = \gamma T^{-3}$ when $n_s \gg 1$.

The largest of the two solution of Eq. (21) is

$$\lambda = \frac{1}{2A} \left(-B + \sqrt{B^2 - 4AC} \right). \quad (23)$$

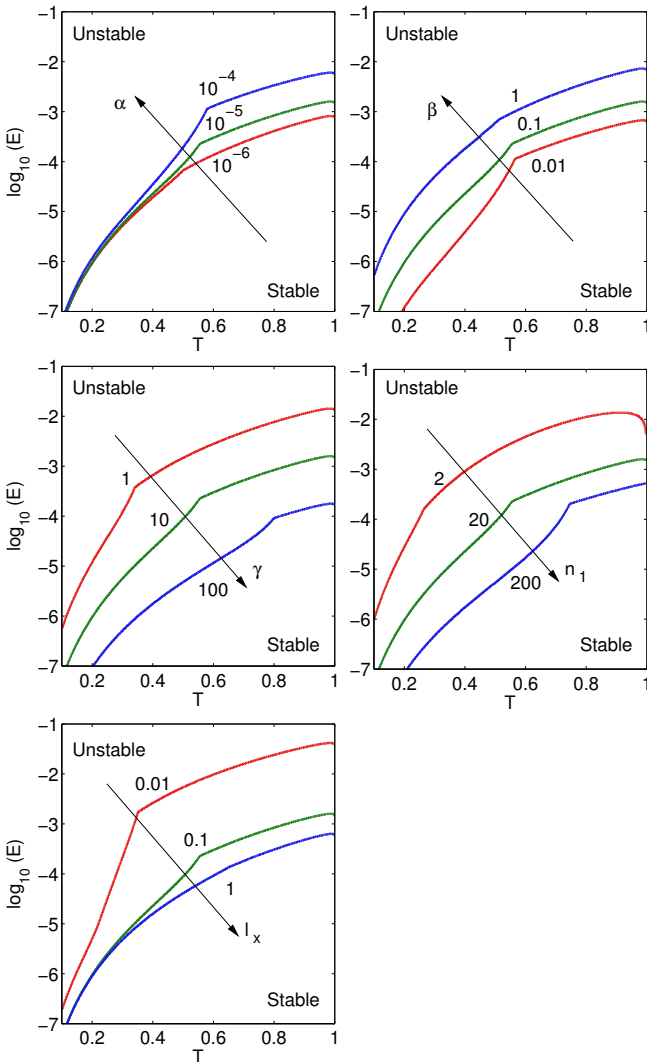


FIG. 2. (color online) The threshold for onset of instability in the $T - E$ plane, calculated as contours of $\max\{\text{Re } \lambda(\mathbf{k})\} = 0$. The state is unstable to the left of the contours and stable to the right. As indicated in the figure, one of the parameters α , β , γ , l_x and n_1 is changed in each panel. In all panels, the middle curve is the same, and it is created with $\alpha = 10^{-5}$, $\beta = 0.1$, $\gamma = 10$, $l_x = 0.1$, $n_1 = 20$.

A mode is linearly stable if $\text{Re } \lambda < 0$ and linearly unstable if $\text{Re } \lambda > 0$, and the threshold condition for instability is $\text{Re } \lambda = 0$. If $B^2 > 4AC$, λ is real, and the threshold condition is $C = 0$. If $B^2 < 4AC$, λ is complex, and threshold condition is $B = 0$. The existence of an imaginary part means that the state will be oscillating. The frequency is $\omega = \text{Im } \lambda = \sqrt{C/A}$.

IV. UNCOATED SUPERCONDUCTOR

In this section we will consider an uncoated superconductor which can be accounted for by putting $\sigma_m = 0$.

A. Instability threshold

Figure 2 shows contours of the instability threshold $\max\{\text{Re } \lambda(\mathbf{k})\} = 0$, with T on the horizontal and E on the vertical axis, obtained by numerical solution of Eq. (23). The instability increment value at the most unstable mode, $\max\{\text{Re } \lambda(\mathbf{k})\}$, is found by iterating over a finite number of k_y values. The value of k_x is fixed as $k_x = \pi/2l_x$.

The panels demonstrate how the instability threshold contours shift when changing α , β , γ , n_1 and l_x . In all panels the middle curves are the same and can be used as a reference. It has the parameter combination $\alpha = 10^{-5}$, $\beta = 0.1$, $\gamma = 10$, $l_x = 0.1$, and $n_1 = 20$.

As expected from both experiments and previous linear stability analysis, the system is stable for low E and high T .^{17,25,27} The system becomes more unstable for increasing values of the Joule heating parameter γ , the creep exponent parameter n_1 , and width of the flux-penetrated region l_x . The system improves stability for increasing values of the lateral heat transport parameter α and parameter for heat transport to the substrate β . The graphs are equally sensitive to β at all T , but most sensitive to α at high T . This indicates that the instability threshold at low T is at longer wavelengths (smaller k_y) in which the lateral heat diffusion is less important. The kinks in the curves occur at $B^2 = 4AC$, which is a transition point to the oscillatory regime.

When $\sigma_m = 0$ we have $J_s = J$, $n_s = n$. Then the coefficients B and C in Eq. (22) simplify to

$$\begin{aligned} B &= k_x^2 + \frac{k_y^2}{n} + \frac{k}{2} \frac{\alpha k^2 + \beta}{nE} J - \frac{k}{2} \frac{J}{J_c} JF, \\ C &= (\alpha k^2 + \beta) \left(k_x^2 + \frac{k_y^2}{n} \right) + (k_x^2 - k_y^2) \frac{J}{J_c} EF. \end{aligned} \quad (24)$$

At low T and E the state is close to what is described by the Bean model, therefore, we let $n \gg 1$, $J = J_c$, and $T = T_0$.

We will now derive closed expressions for the threshold electric field, $E_{\text{th}}(T, k_x)$, in three limiting cases.

0. Uniform oscillatory instability. At low electric fields the onset of instability takes place in a thin layer along the edge, so that $k_x^2 \gg 1, k_y^2$. In this case $B^2 \leq 4AC$ and the solutions of the dispersion equation $\text{Re } \lambda = 0$ are oscillatory. The instability onset in this case corresponds to $B = 0$, or

$$B = k_x^2 + \frac{k_x}{2} \frac{\alpha k_x^2 + \beta}{nE} J_c - \frac{k_x}{2} J_c F = 0. \quad (25)$$

Solving this equation for E gives the threshold electric field

$$E_{\text{th}}^{(0)} = \frac{J_c}{n} \frac{\alpha k_x^2 + \beta}{J_c F - 2k_x}. \quad (26)$$

The physical interpretation of Eq. (26) is straightforward: increasing heat removal through α and β increase the

threshold, while increasing Joule heating through F and nonlinearity through n decrease it.

In the Bean model limit, $n \rightarrow \infty$, the threshold is independent of α and β . This corresponds to the adiabatic limit:

$$k_x^{(\text{adiab})} = J_c F / 2. \quad (27)$$

This means that the sample is always stable for $l_x < \pi/2k_x^{(\text{adiab})} = \pi/J_c F$.

1. Finite-wavelength oscillatory instability. At higher temperatures and higher electric fields the instability will nucleate at smaller k_x and the most unstable mode will be at finite k_y . Still k_x and k_y are comparable in size so that the instability is accompanied by oscillations. This means that the condition for onset of instability is $B = 0$ in Eq. (24). When neglecting the k_y^2/n term, it becomes

$$B = \frac{J_c}{2nE} \alpha k^3 + \frac{1}{2} \left(\frac{J_c \beta}{nE} - J_c F \right) k + k_x^2 = 0. \quad (28)$$

The most unstable mode is found by the condition $\partial \text{Re } \lambda / \partial k_y = 0$, which gives $\partial B / \partial k_y = 0$, i.e.,

$$k = \sqrt{\frac{nE}{3\alpha}} \sqrt{F - \frac{\beta}{nE}}. \quad (29)$$

Elimination of k_y leads to

$$\frac{J_c}{3} \sqrt{\frac{nE}{3\alpha}} \left(F - \frac{\beta}{nE} \right)^{3/2} - k_x^2 = 0. \quad (30)$$

This equation straightforwardly gives the onset condition in terms of the threshold k_x . However, in this work we focus on the threshold electric field, so the equation must be solved for E . Changing variables to $x = (\beta/FnE)^{1/3}$ gives a cubic equation $x^3 + 3px + 2q = 0$, with the coefficients $p = (J_c F)^{-2/3} (\alpha/\beta)^{1/3} k_x^{4/3}$ and $q = -1/2$. This is solved with Cardano's formula $x = u_+ + u_-$, where

$$u_{\pm} = \left[\frac{1}{2} \pm \sqrt{\frac{1}{4} + \frac{\alpha}{\beta} \frac{k_x^4}{(J_c F)^2}} \right]^{1/3}.$$

Thus, the threshold electric field for finite-wavelength oscillatory instability is

$$E_{\text{th}}^{(1)} = \frac{\beta}{Fn} (u_+ + u_-)^{-3}. \quad (31)$$

Due to the approximations used in the derivation, the expressions is mainly of value for small k_x . Series expansion gives

$$E_{\text{th}}^{(1)} = \frac{\beta}{Fn} \left[1 + 3 \left(\frac{\alpha}{\beta} \frac{k_x^4}{J_c^2 F^2} \right)^{1/3} \right]. \quad (32)$$

The peculiar $k_x^{4/3}$ dependency is due to the $k/2$ Biot-Savart kernel and is thus a consequence of the nonlocal electrodynamics.

2. Fingering instability. When the temperature is sufficiently high the oscillations cease to exist and the instability is elongated transverse to the edge with $k_y \gg k_x$. It is thus called a fingering instability and the condition for onset is $C = 0$ in Eq. (24):

$$C = (\alpha k_y^2 + \beta) \left(k_x^2 + \frac{k_y^2}{n} \right) - EF k_y^2 = 0. \quad (33)$$

The most unstable mode is at $\partial \lambda / \partial k_y = 0$, giving $\partial C / \partial k_y = 0$. Hence,

$$2\alpha k_y^2 = nEF - n\alpha k_x^2 - \beta. \quad (34)$$

Eliminating k_y and solving for E gives the threshold electric field for the fingering instability

$$E_{\text{th}}^{(2)} = \frac{1}{F} \left(\sqrt{\alpha} k_x + \sqrt{\frac{\beta}{n}} \right)^2. \quad (35)$$

This is the same expression as found in Refs. 24 and 25.

In order to compare the above threshold conditions with experiments, they must typically be reformulated with the variables H_a , \dot{H}_a , and T_0 , rather than E , T , and k_x . This mapping is beyond the scope of the present work, but we will outline how it can be done.

The threshold applied magnetic field can be found by mapping $k_x = \pi/2l_x$ where $l_x(H_a)$ is the flux penetration depth from the Bean model. At the same time $E = E(H_a, \dot{H}_a)$.⁴³ For low E , we have $T \approx T_0$. The threshold temperature can be defined as the temperature where $l_x = 1$, i.e., full penetration is reached without the instability being nucleated. In this limit the dominant mechanism for prevention of the instability is the heat transfer to the substrate. Hence, a simple approximation for the threshold temperature can be obtained by $k_x \rightarrow 0$. Then all three cases, [Eqs. (26), (32), and (35)], give the same condition: $E = \beta/nF$.

B. The stability diagram

Figure 3 shows a linear stability diagram in the $T-E$ plane, calculated from Eq. (23), with parameters $\alpha = 10^{-5}$, $\beta = 0.1$, $\gamma = 10$, $n_1 = 20$, and $l_x = 0.1$. White color corresponds to values of T and E where $\max\{\text{Re } \lambda(\mathbf{k})\} < 0$, i.e., in the white regions the distributions are stable. In the figure, there are two stable regimes. The lower one is the low-dissipative flux creep state, which is stable for $E < E_{\text{th}}(T)$. The upper is the high-dissipative flux-flow regime, which is stable for $E > J_c(T)$, i.e., when the $J-E$ curve is linear, see Eq. (3). These two stable domains are separated by an unstable region, where the arrow is meant to remind us that for the unstable state, E and T are bound to increase with time.

The color in the diagram describes the properties of the most unstable mode: red is uniform ($k_y = 0$), while

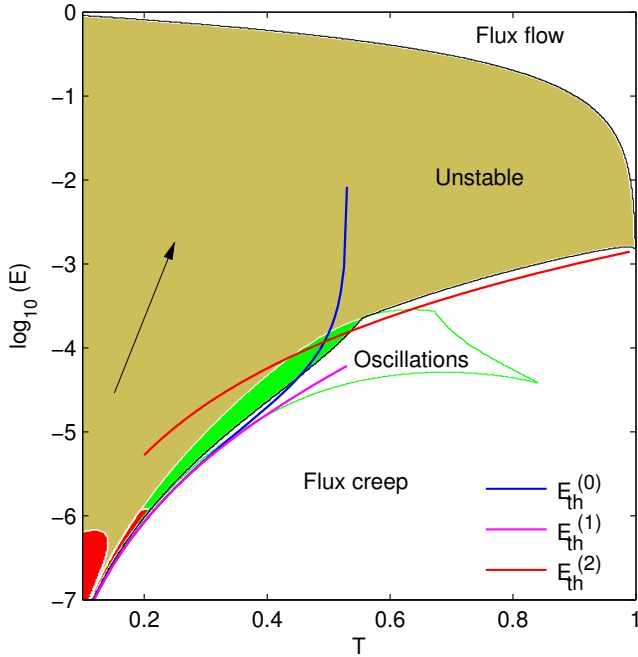


FIG. 3. (color online) Stability properties of the superconductor in the $T - E$ plane. White denotes stable, coloured unstable. Red, green and yellow, means uniform oscillatory, non-uniform oscillatory, and fingering instability, respectively. The solid curves are $E_{\text{th}}^{(0)}$, $E_{\text{th}}^{(1)}$, and $E_{\text{th}}^{(2)}$. Parameters are $\alpha = 10^{-5}$, $\beta = 0.1$, $\gamma = 10$, $l_x = 0.1$, $n_1 = 20$.

green and yellow are non-uniform ($k_y > 0$). Both the green and the red are modes giving oscillations ($\text{Im } \lambda \neq 0$). The colored lines correspond to the Eqs. (26), (32) and (35) derived, respectively, for limiting cases 0, 1 and 2. As expected from the conditions of derivation, $E_{\text{th}}^{(0)}(T)$ and $E_{\text{th}}^{(1)}(T)$ follow nicely the edge of instability at low T . This means that at low T , the nucleated instability should be uniform, or close to uniform. At high enough T , the most unstable mode is at finite wavelength, i.e., it should give rise to fingering structures. As expected, the instability threshold in this case is nicely approximated by $E_{\text{th}}^{(2)}(T)$.

Inside the instability region, we have not derived any analytical expressions, since the linearized equations are not valid far from the instability threshold. However, it is possible to extract some qualitative information from the diagram also in this case. Of particular interest is that most of the diagram is yellow, which indicates that modes with $k_y > 0$ will grow fastest after the instability has been nucleated.

The green line encloses the part of the diagram where the most unstable mode has $\text{Im } \lambda \neq 0$. i.e., it might be possible to detect damped oscillations.

C. Simulations

The simulations were carried out in two steps, as described in Sec. II. First, the background state was prepared with thermal feedback turned off, giving uniform $T = T_0$. Second, the thermal feedback was turned on, and the perturbation δT started evolving.

Figure 4 shows successive T -maps at times $t_1 < t_2 < t_3 < t_4$ after the thermal feedback was turned on, for two separate runs with $T_0 = 0.15$ (left) and $T_0 = 0.4$ (right). We used the following values of the parameters: $\gamma = 10^{-5}$, $\beta = 0.1$, $\gamma = 10$, $l_x = 0.2$, and $n_1 = 20$. The ramp rates were chosen as $\dot{H}_a = 4 \cdot 10^{-7}$ and $5 \cdot 10^{-5}$ for $T_0 = 0.15$ and 0.4 , respectively. Both values are just above the instability thresholds found heuristically by varying \dot{H}_a .

At $t_1 = 10$ the temperature is elevated in the flux-penetrated region. Even though the temperature rise is rather small, the instability is already nucleated and the appearance of a dendritic flux avalanche inevitable. For $T_0 = 0.15$ the heated region is a narrow band near the edges, while for $T_0 = 0.4$ it is much wider and extends almost to the flux front.

The panels at t_2 show the T -maps when the flux-flow hot spots appear. Each panel has only one hot spot, which is characterized by having the highest temperature. At this early time it is still not much higher than the surroundings, and hence just barely visible. The hot spots appear because J_c decreases faster than J and eventually some position reaches the flux-flow condition $J = J_c$. The two runs develop at different rates, so we have $t_2 = 28$ for $T_0 = 0.15$ and $t_2 = 12.5$ for $T_0 = 0.4$. Because the hot spots are characterized by the high flux-flow resistivity, they will quickly heat to the superconductivity transition temperature. The locations of the hot spots are random, due to the uniformity of the sample.

At $t_3 = t_2 + 0.5$ the avalanches have reached the propagation stage, where the hot spots have transformed to thin fingers. The fingers are either in the flux-flow or normal phase, and due to the high dissipation characterized by extremely rapid propagation. The propagation is driven by the tip being adiabatically converted from the critical or Meissner state to the flux-flow state. At this stage, the propagation speed is not limited by thermal effects, so the speed of the front can even exceed the sound velocity.^{30,45}

The final frames at $t_4 = t_2 + 10$ show the large branching structures. The avalanches have reached their full extent and the structures are about to disappear as the heat is absorbed by the substrate. The dendritic structures will remain in B_z and J .³¹

Figure 4 allows us to present a fairly complete picture of how dendritic flux avalanches are nucleated and how they evolve. The avalanche has two distinct stages. In the first stage, the dynamics is characterized by the thermomagnetic instability driven by a nonlinear $I-V$ curve. Even though both E and T increase in time, they remain quite uniform. In the second – propagation – stage the

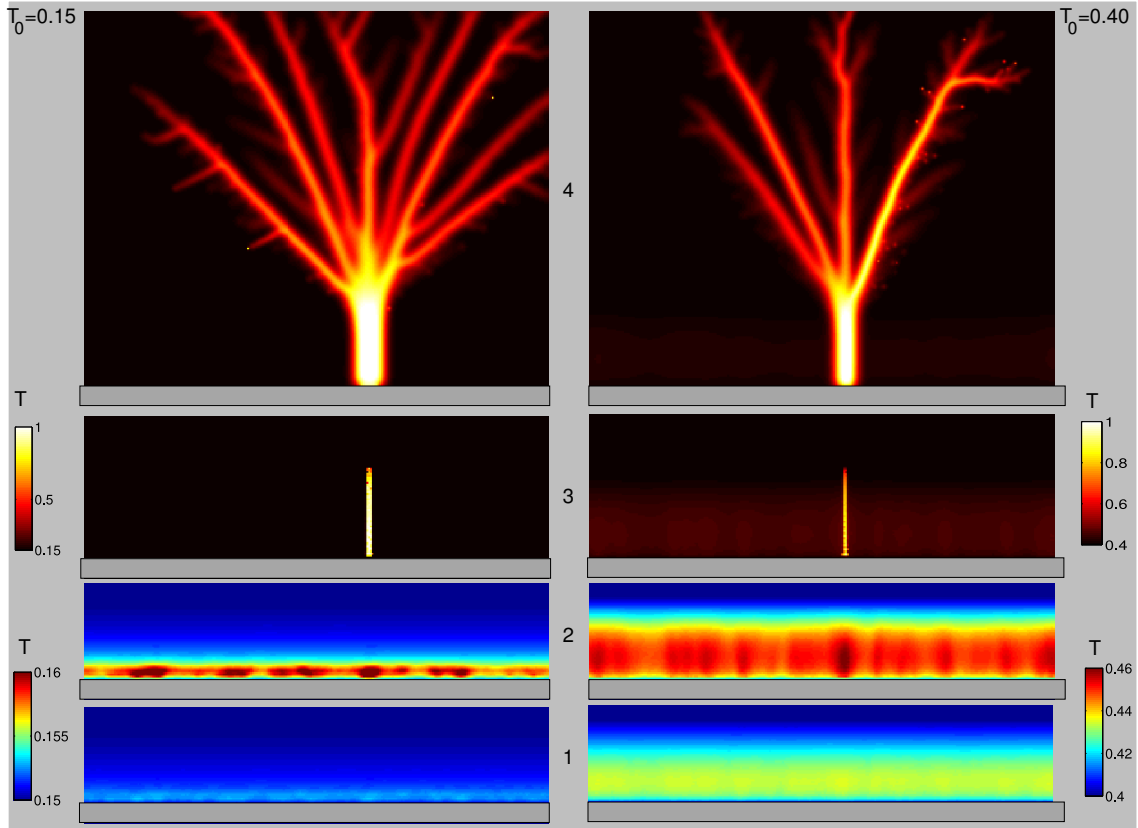


FIG. 4. (color online) Evolution of dendritic flux avalanches, with $T_0 = 0.15$ (left) and $T_0 = 0.4$ (right). The temperature maps are at times $t_1 < t_2 < t_3 < t_4$, simulated with parameters $\alpha = 10^{-5}$, $\beta = 0.1$, $\gamma = 10$, $l_x = 0.2$, $n_1 = 20$.

dendritic flux structure is created. The dynamics is now totally driven by the highly dissipative (either flux-flow or normal-state) branching structure invading the inner superconducting part of the sample.

It is worth paying attention to the time spent in the two stages. The avalanche at $T_0 = 0.15$ takes 28 time units in its first part to increase the temperature up to $T = 0.16$. In the propagation stage, it rises to $T \sim 1$ in less than 0.5 time units, and the creation of the branching structure takes 10 time units. This means that the actual instant of nucleation of the avalanche is much earlier than its first unambiguous signatures, such as the hot spot, or high pulses of T and E .

Non-locality of the electrodynamics plays an essential role in the transition between the stages because it allows a uniformly nucleated instability to develop into a non-uniform avalanche. This behavior is different from parallel geometry, where the interaction between modes is absent, and a uniformly nucleated instability typically develops into a global flux jump.⁶

D. Comparison of the results

Let us now compare the results of the simulations with the predictions of the linear stability analysis, us-

ing identical parameters. Figure 5 presents a stability diagram in the T - E plane. Again, white regions are stable and yellow ones are unstable according to the linear stability analysis. Here we do not distinguish different kinds of instability. The dots in the figure correspond to $\{T_{\max}, E_{\max}\}$ pairs extracted from the runs shown in Fig. 4. For each time, we collect the maximum temperature T_{\max} and the electric field E_{\max} at the same time and position. Inside the instability region the points are ordered in time since $T_{\max}(t+\Delta t) > T_{\max}(t)$. This means that we can follow the evolution of the instability as a trajectory in the T - E diagram. The numbers correspond to the panels in Fig. 4 and link subsequent stages of the development to the temperature distributions.

The onset of instability is the E_{\max} with the lowest value. At $T_0 = 0.15$ the lowest E_{\max} is very close to the instability threshold calculated by the linear stability analysis. At $T_0 = 0.4$ the lowest E_{\max} is somewhat higher than the threshold. Hence we can say the linear stability analysis gives a good, but conservative, estimate for the actual instability onset.

When the avalanche reaches the propagation stage, the trajectory $\{T_{\max}, E_{\max}\}$ makes a strong turn since $E_{\max} \sim J_c(T_0)$ has reached its maximum value while T_{\max} increases with even faster rate. The maximum temperature (not shown in the figure) is reached when the heat

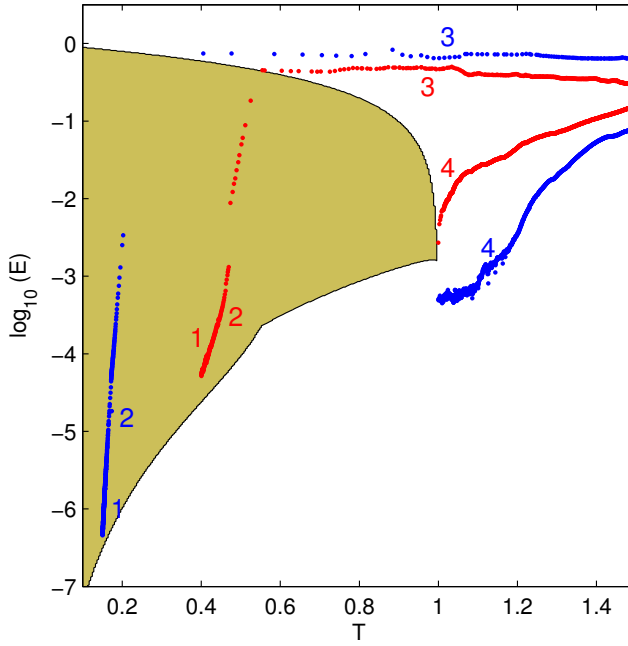


FIG. 5. (color online) The development of an avalanche compared with the stability properties. Yellow means linearly unstable and white means stable. The points $\{T_{\max}, E_{\max}\}$ are extracted from the numerical simulations. The blue points are for $T_0 = 0.15$, red for $T_0 = 0.4$. The labels 1-4 refer to the temperature distributions of Fig. 4. Parameters are $\alpha = 10^{-5}$, $\beta = 0.1$, $\gamma = 10$, $l_x = 0.2$, $n_1 = 20$.

removal is able to balance the heat production. After that, the temperature and electric field decrease with relatively slow rates until $T_{\max} = 1$ and $E_{\max} \ll 1$. The system is then again in the stable flux creep state and the avalanche is over. Then E_{\max} will drop to a very low value, $E_{\max} \ll H_a$,³⁰ and T_{\max} will decrease with a rate determined by the Newton cooling in Eq. (6) until $T_{\max} = T_0$.

V. METAL-COATED SUPERCONDUCTOR

We will now consider how the thermomagnetic stability is affected by an adjacent normal-metal film. As depicted in Fig. 1, the metal layer is close, but not in a thermal contact with the superconductor. The linear stability analysis of this model was done in Sec. II.

A. Dependence on the metal conductivity

Let us first consider what happens when changing the normal metal conductivity σ_m . Figure 6 shows the contours $\max\{\text{Re } \lambda(\mathbf{k})\} = 0$ for $\alpha = 10^{-5}$, $\beta = 0.1$, $\gamma = 10$, $l_x = 0.1$, $n_1 = 20$. The contours are calculated by numerical solution of Eq. (23); the curves correspond to different σ_m . The figure shows that the size of the unsta-

ble region shrinks significantly when σ_m is increased from 0 to 100. As expected, the metal layer mainly affects the stability at high E and T , when the conductivities of the two layers are within the same order of magnitude.

Of particular importance is that Fig. 6 predicts a threshold temperature T_1 , indicated by dotted vertical lines in the figure. Above this temperature the system is stable no matter the value of E . This opens a possibility that an avalanche can terminate without heating the sample above T_c . Thus the bistable properties of the system depend crucially on the value of T_1 , which, in turn, depends on σ_m . For example, $\sigma_m = 1$ gives $T_1 = 0.97$. In this case, a dendritic flux avalanche will most likely develop in the same way as without a metal layer. For $\sigma_m = 10$, we have $T_1 = 0.8$, which gives some prospects of avalanches terminating without the superconductor being heated above T_c . For the highest conductivity, $\sigma_m = 100$, we have $T_1 = 0.5$, which means that it is likely that the magnetic braking will suppress formation of dendritic flux structures.

Note that T_1 is fundamentally different from the threshold temperature, T_{th} , often observed experimentally.²⁵ In particular, the threshold described by T_{th} is a consequence of the rapid growth of the thermal parameters. It depends on E , and does not alter the bistable properties of the system.

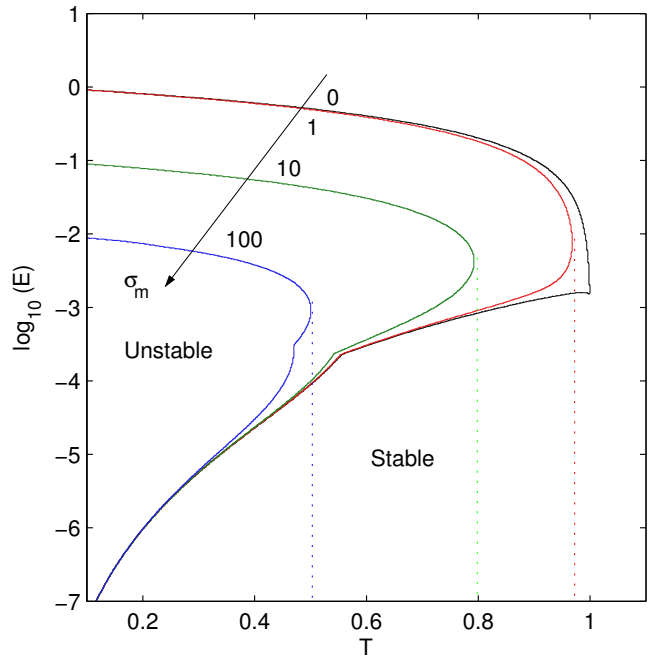


FIG. 6. (color online) The effect of changing the normal metal conductivity. The stability threshold contours in the $T-E$ plane, for $\sigma_m = 0, 1, 10$, and 100 . Increasing metal layer conductivity improves stability at high E and T . Parameters are $\alpha = 10^{-5}$, $\beta = 0.1$, $\gamma = 10$, $l_x = 0.1$, $n_1 = 20$.

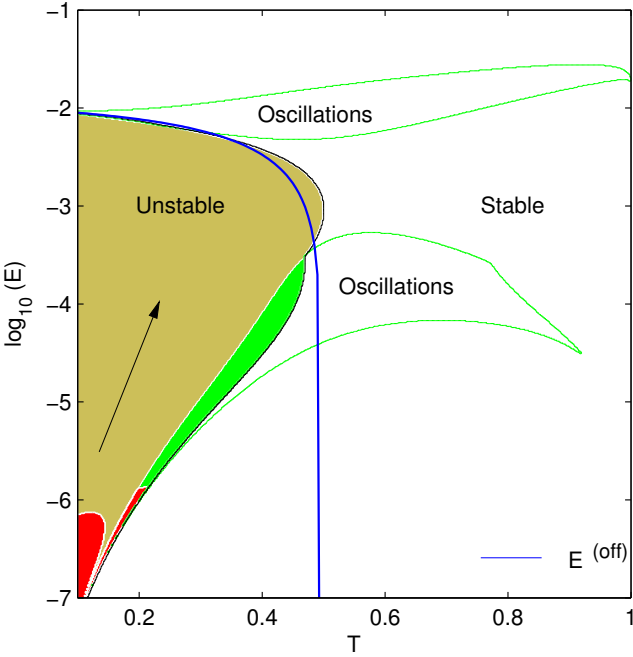


FIG. 7. (color online) Stability properties of the metal-coated superconductor in the $T - E$ plane. White denotes stable, coloured unstable. Red, green and yellow, means uniform oscillatory, non-uniform oscillatory, and fingering instability, respectively. The solid curve is $E^{(\text{off})}$. Parameters are $\sigma_m = 100$, $\alpha = 10^{-5}$, $\beta = 0.1$, $\gamma = 10$, $l_x = 0.1$, $n_1 = 20$.

B. Threshold for offset of the instability

Let us now derive analytical expressions for the conditions for offset of the instability at high E and T . We assume that E and T are constant solutions of the nonlinear equations, so that Eq. (22) can be used as a formal solution of the linearized equations in Fourier space. At the high electric fields, the background state may have evolved significantly from what is described by the Bean model, and the solution can be non-stationary, typically with $T \gg T_0$ and $E \gg \dot{H}_a$.

The magnetic braking comes into play when the nonlinear exponent of the composite system, n from Eq. (15), is reduced. When $n_s J_m \gg J_s$, we have

$$n = 1 + J_s/J_m, \quad (36)$$

where $J_m = \sigma_m E$ and $J_s \approx J_c$, when $n_s \gg 1$.

Several modes may be important for the offset of instability. We will here focus on uniform oscillatory modes, which can be found by solving $\text{Re } \lambda = 0$ with $k_y = 0$. Hence,

$$B = k_x^2 + \frac{k_x}{2} (\alpha k_x^2 + \beta) \sigma_m - \frac{k_x}{2} (J_c - \sigma_m E) F = 0. \quad (37)$$

Solving for E gives

$$E^{(\text{off})} = \frac{1}{\sigma_m} \left(J_c - \frac{2k_x}{F} \right) - \frac{\alpha k_x^2 + \beta}{F}. \quad (38)$$

The offset of instability is thus appearing at high electric fields, of the order of $E \sim J_c/\sigma_m$.

C. The stability diagram

Figure 7 shows a $T - E$ stability diagram calculated by numerical solution of Eq. (23) with $\sigma_m = 100$. Other parameters are the same as in Fig. 3. As in the previous plot, white is stable, red is uniform oscillatory, green is nonuniform oscillatory, and yellow is fingering instability. For low T and E , the result is just as for the uncoated sample. Consequently, the low- T threshold conditions for onset of instability, $E_{\text{th}}^{(0)}$ and $E_{\text{th}}^{(1)}$, should be valid also for the metal-covered sample. For high T or E , the differences compared to the uncoated sample are substantial. According to the diagram, at $E > J_c/\sigma_m$ and $T > T_1 \sim 0.5$ the system is stable.

The upper edge of the instability region is offset of the instability, where all modes become stable. Yet, many modes will have values $\text{Re } \lambda \approx 0$ which means that they are almost stationary. We thus expect that avalanches subjected to magnetic braking will give rise to oscillations with long lifetimes in electric field and temperature.

The analytical curve, Eq. (38), derived on the assumption of long wavelengths, provides a very good fit for the instability offset threshold, except for the temperatures close to T_1 .

D. Simulations

Figure 8 shows temperature distributions at times $t_1 < t_2 < t_3 < t_4 < t_5$ obtained by numerical simulations. Except the presence of the metal layer with $\sigma_m = 100$, the calculation procedure and the initial parameters are identical to those used in Fig. 4. The times t_1 to t_4 are the same as in Fig. 4, while the last frame is at a much later time, $t_5 = t_2 + 30$. The time evolution of the two runs with $T_0 = 0.15$ and $T_0 = 0.4$ are quite different, so we discuss them separately.

For $T_0 = 0.15$, the states at t_1 and t_2 are exactly the same as for the previous run with the uncoated sample. This means initial phase of the avalanche is not affected by the metal layer. At t_3 , a hot spot heated to $T \approx 0.25T_c$ is visible. It is propagating away from the edge, but much more slowly than the propagating finger of Fig. 4. At t_4 , the state has deviated further from that for the uncoated sample and there are even two fingers developing in parallel. The temperature inside the fingers is approximately $T \sim 0.5$. The final frame shows the temperature distribution at $t_5 = t_2 + 30$, which is more or less the final development of the instability. The two structures have at this point exceeded the flux front but they are still much smaller than the dendritic flux avalanche in Fig. 4.

For $T_0 = 0.4$, the temperature distribution at nucleation is the same as in the uncoated sample. However, all times $t > t_1$ are affected by the magnetic braking.

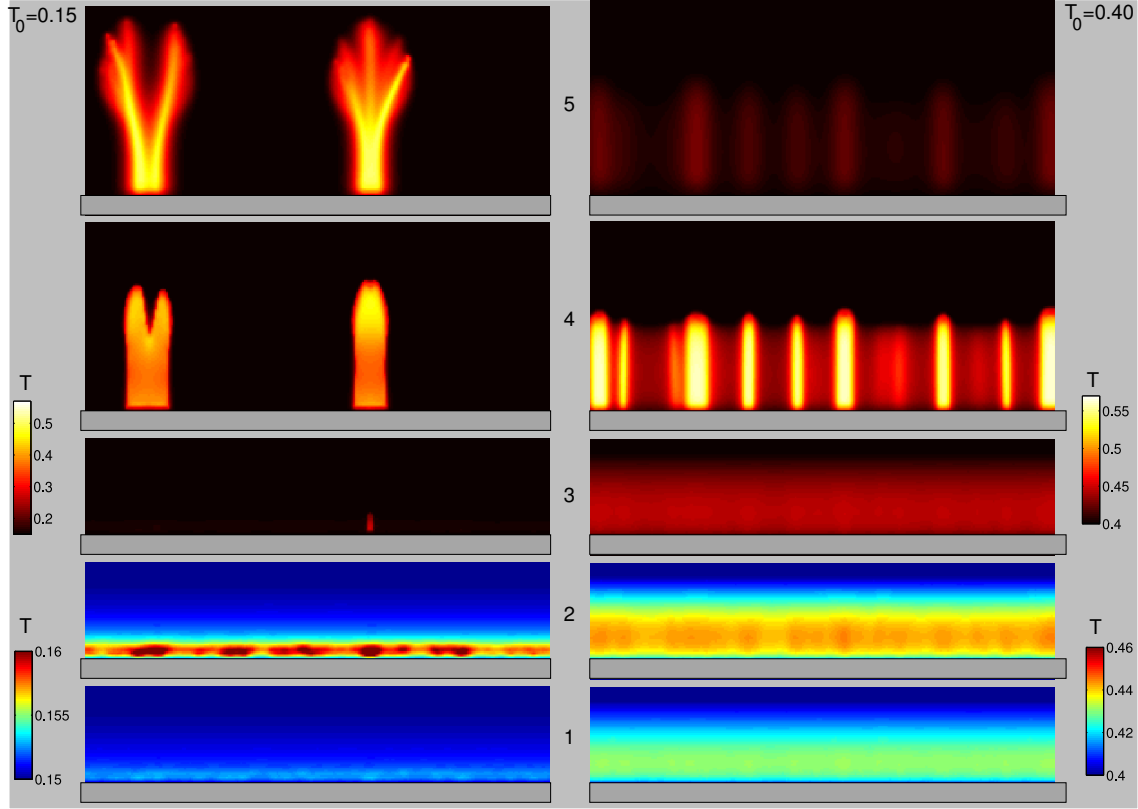


FIG. 8. (color online) Evolution of flux avalanches subjected to magnetic braking, with $T_0 = 0.15$ (left) and $T_0 = 0.4$ (right). The temperature maps are at times $t_1 < t_2 < t_3 < t_4 < t_5$, simulated with parameters $\alpha = 10^{-5}$, $\beta = 0.1$, $\gamma = 10$, $l_x = 0.2$, $n_1 = 20$.

In the figure, it is impossible to identify one individual avalanche. Instead, there is a quasi-periodic structure, in which the peaks are heated to $T \sim 0.56$. The structures are mainly in the critical state region and do not penetrate into the Meissner state region. In the last frame taken at $t_5 = t_2 + 30$ the temperature is almost back to T_0 .

The comparison between Figs. 4 and 8 show that, for $T_0 < T_1$ and $E \ll J_c/\sigma_m$, the initial stage of the instability development is not affected by the presence of a metal layer. However, with high metal layer conductivity, the magnetic braking prevents the rapid propagation of avalanches, and as a result the final structure of the avalanche is strongly altered. The avalanche at $T_0 = 0.15$ looks like a blob, with some tendency of branching, while at $T_0 = 0.4$ it becomes a semi-periodic wiggling of the flux front. In both cases, the magnetic braking prevents formation of the dendritic structure.

E. Comparison of the results

In order to check the accuracy of the predictions of the linear stability analysis, let us compare them with the results of simulation using identical parameters. Figure 9 shows a $T - E$ stability diagram, where the background

color represents results of the linear stability analysis, so that white means stability, yellow instability. The points are $\{T_{\max}, E_{\max}\}$ pairs extracted from the simulations. T_{\max} is the highest temperature at a given time and E_{\max} is the electric field at the same time and location. The blue points come from the run nucleated at $T_0 = 0.15$, red points at $T_0 = 0.4$. The numbers 1-5 correspond to the panels in Fig. 8.

At $T_0 = 0.15$, the instability is nucleated at low E and between t_1 to t_2 , both T and E grow with time, exactly as without metal coating. At t_3 , the electric field saturates at $E \sim J_c/\sigma_m$, Eq. (38), which is much lower than the saturation level $E \sim 1$ in the pristine superconductor of Fig. 5. The fit with the linear stability analysis is remarkable as $\{T_{\max}, E_{\max}\}$ follows the edge of the diagram. At $t > t_5$, the electric field and temperature drop, and the avalanche is over. This means that the simulated avalanche to large extent behaves as predicted by the linear stability analysis.

The temperature $T_0 = 0.4$ is close to $T_1 \sim 0.55$. Hence, the $\{T_{\max}, E_{\max}\}$ points are close to the instability threshold at all times, and the trajectory deviates strongly from that of the pristine superconductor of Fig. 5. The electric field grows until it hits the maximum at $E \sim J_c/\sigma_m$, whereupon the electric field stays constant for some time while T increases. At t_4 , the

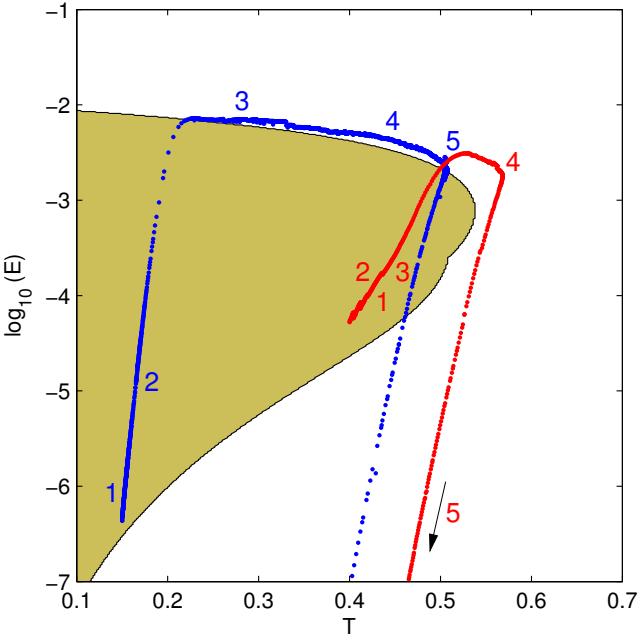


FIG. 9. (color online) The development of avalanches compared with the stability properties for a metal-coated sample. Yellow means unstable, white stable. The points $\{T_{\max}, E_{\max}\}$ are extracted from simulations: the blue points are for $T_0 = 0.15$, red for $T_0 = 0.4$. The labels 1 – 5 refer to the temperature distributions of Fig. 8. Parameters are $\sigma_m = 100$, $\alpha = 10^{-5}$, $\beta = 0.1$, $\gamma = 10$, $l_x = 0.2$, $n_1 = 20$.

avalanche has reached its largest extent and the temperature and electric field decrease rapidly. At time t_5 the electric field is so low that it is out of the range of the figure.

Because the avalanches at the propagation stages follow the edges of the instability region, we can conclude that the linearized theory describes properly also the offset of instability due to the magnetic braking.

VI. DISCUSSION AND SUMMARY

Type II superconducting films in the critical state are susceptible for the thermomagnetic instability, which may cause dendritic flux avalanches. Such avalanches are potentially damaging for applications. Consequently, it is desirable to work out criteria telling when the instability appears and how its impact can be minimized. Derivation and analysis of those criteria for superconducting films (both uncoated and coated by a normal metal) was the purpose of the present work. To reach this goal we have performed both linear stability analysis and numerical simulations of the equations governing onset and propagation of coupled fluctuations of magnetic flux and temperature. Comparison of these results reveal the physical picture of the flux avalanche dynamics in thin-film superconductors.

The state prior to linearization was quantified by the electric field E and temperature T . Perturbations of this state were analyzed in the Fourier space, their scales having been quantified by wave vector \mathbf{k} . We considered the most unstable modes with \mathbf{k} corresponding to the largest instability increment, $\max\{\text{Re } \lambda(\mathbf{k})\}$. In x direction, the most unstable mode is always the one with shortest wavelength, and thus the most unstable mode was associated with the flux penetration depth $l_x = \pi/2k_x$. The material properties were combined into the dimensionless heat conductivity α , the dimensionless coefficient of heat transfer to the substrate β , the Joule heating parameter γ , and the flux creep exponent parameter n_1 . These quantities depend only on measurable parameters, therefore the theory is quantitative. The derived expressions were explored under assumption of realistic, for conventional superconductors and MgB₂, temperature dependencies of the material parameters.

The linear stability analysis showed that the superconductor was stable for small E and l_x , and high T , in agreement with previous results. Increased γ and n_1 decreased stability and increased α and β improved stability. Analytical expression where derived in three cases: (i) uniform oscillatory instability for small T , E , and l_x ; (ii) nonuniform oscillatory instability for intermediate T and E and for large l_x ; (iii) fingering instability for higher T and E .

We have solved the same set of equations numerically, but without linearization and with more realistic boundary conditions. The initial state was numerically prepared by ramping of the applied magnetic field, with thermal feedback tuned off. At a given flux penetration depth, the thermal feedback was turned on, and the evolution of the perturbation was explored. We report the results for parameter combinations just above the heuristically found instability threshold, where the instability developed into a dendritic flux avalanche. We have found that the avalanche has two distinct stages. First, just after the nucleation, the sample is in the flux creep state, and even though T and E increased exponentially with time, the perturbations are almost uniform. Since E is low, the flux traffic is limited. Second, the propagation stage begins with the appearance of a hot spot in the flux-flow phase. The hot spot soon turns into a thin finger, which rapidly propagates into the sample, creating a branching structure. Hence, we conclude that the avalanche is initiated by the thermomagnetic instability, but this is not the main mechanism behind creation of the dendritic structure. Instead, it is more accurate to think about the dendritic structure as created by a highly-dissipative phase (flux-flow or normal) invading a low-dissipative one (flux creep or Meissner).

For two different temperatures, the instability onset found heuristically based on numerical simulations was at slightly higher electric fields than those predicted by the linearized theory. Therefore, the linear stability analysis should provide a good, but conservative, estimate of the instability threshold.

The magnetic braking was described by a simple model where the superconducting and metallic layers were considered as two electrically and thermally isolated current-carrying layers connected in parallel.

Linearization of the set of equations for the coated system gave two new parameters: the normal metal sheet conductivity σ_m and the nonlinearity exponent of the composite system $n = n(E, T)$. For low T and E the conditions for onset of instability were unchanged by the presence of the metal layer. At higher E , when $n_s J_m \gg J_c$, the limit for offset of instability was lowered by the presence of the metal. The effect was stronger for increasing σ_m . The theory predicts that there is a temperature $T_1(\sigma_m) < T_c$, such that the system is stable for any E when $T > T_1$. This means that the system can recover from an instability without being heated to the normal state. Analytical expressions for offset of the uniform oscillatory instability by magnetic braking were derived in the low temperature limit.

Numerical simulations confirmed the prediction of the linear stability analysis that the impact of avalanches may be significantly reduced by magnetic braking. The avalanches subjected to magnetic braking created extended protrusions of the flux front rather than dendritic structures. The reason for the suppression of the flux traffic is that finite conductivity of the coating layer limits the electric field. The maximum temperature during the avalanches in a coated film did not exceed T_c , just as predicted by the linearized theory.

The main conclusions from this work are that a uniform thermomagnetic instability can develop into a dendritic flux avalanche. In the long, initial phase of the avalanche, the electromagnetic non-locality causes the appearance of a small non-uniformity in the temperature perturbation. A dendritic structure is created when a hot spot appears in a random position, and develops into a finger, which propagates away from the edge, at very high velocity. The magnetic braking does not affect the nucleation of the thermomagnetic instability at low

electric fields, but it may significantly reduce the impact of avalanches, and may suppress formation of dendritic structures.

Several predictions from this work can be checked experimentally. The prediction that the instability at low temperatures is nucleated uniformly along the edge is not easy to check directly, since it is very difficult to distinguish a stable configuration from an unstable one in avalanches at early times. Instead, one can look for collective oscillations, e.g., by using an array of Hall probes along the edge, since oscillations are the hallmarks of modes with $k_y < k_x$. The formulas for the instability threshold could be checked indirectly, by finding and fitting values for the threshold length $l_x(H_a)$ with experimental values. To check the theory for offset of instability by magnetic braking one could also use an array of Hall probes, this time at the edge of a superconducting strip covered by metal. The electric field observed during the avalanche should be inversely proportional to the sheet conductivity of the normal metal. The frequencies $\omega = \sqrt{C/A}$ of the undamped oscillations also bear information of physical parameters of the system.

The theory can be modified to handle the case when the metal layer and superconductor are in a close thermal contact. In this limit, the thermal shunt should shift the onset of instability, because normal metals have $\kappa_m \propto T$ and $c_m \propto T$ at low temperatures. The magnetic braking should, however, be less efficient than the case considered in this work, since the Joule heating in the normal metal will also heat the superconductor. Therefore, the Joule heating term should be enlarged from $j_s E$ to $j E$. In the general case one must model the temperature in the superconductor and normal metal separately.

ACKNOWLEDGMENTS

This work was financially supported by the Research Council of Norway.

-
- ¹ C. P. Bean, Rev. Mod. Phys. **36**, 31 (1964).
- ² A. M. Campbell and J. E. Evetts, Adv. Phys. **21**, 199 (1972).
- ³ E. H. Brandt, Rep. Prog. Phys. **58**, 1465 (1995).
- ⁴ S. L. Wipf, Phys. Rev. **161**, 404 (1967).
- ⁵ P. S. Swartz and C. P. Bean, J. Appl. Phys. **39**, 4991 (1968).
- ⁶ R. G. Mints and A. L. Rakhmanov, Rev. Mod. Phys. **53**, 551 (1981).
- ⁷ S. L. Wipf, Cryogenics **31**, 936 (1991).
- ⁸ Y. B. Kim, C. F. Hempstead, and A. R. Strnad, Phys. Rev. **129**, 528 (1963).
- ⁹ P. Leiderer, J. Boneberg, P. Brüll, V. Bujok, and S. Herminghaus, Phys. Rev. Lett. **71**, 2646 (1993).
- ¹⁰ I. L. Maximov, Physica C **235-240**, 3017 (1994).
- ¹¹ V. Vlasko-Vlasov, U. Welp, V. Metlushko, and G. W. Crabtree, Physica C **341**, 1281 (2000).
- ¹² A. V. Gurevich and R. G. Mints, Rev. Mod. Phys. **59**, 941 (1987).
- ¹³ K.-H. Müller and C. Andrikidis, Phys. Rev. B **49**, 1294 (1994).
- ¹⁴ M. N. Wilson, C. R. Walters, J. D. Lewin, and P. F. Smith, J. Phys. D **3**, 1571 (1970).
- ¹⁵ M. G. Kremlev, Zh. Eksp. Teor. Fiz. Pis'ma Red. **17**, 312 (1973).
- ¹⁶ R. G. Mints and A. L. Rakhmanov, J. Phys. D **8**, 1769 (1975).
- ¹⁷ A. L. Rakhmanov, D. V. Shantsev, Y. M. Galperin, and T. H. Johansen, Phys. Rev. B **70**, 224502 (2004).
- ¹⁸ L. Legrand, I. Rosenman, C. Simon, and G. Collin, Physica C **211**, 239 (1993).
- ¹⁹ R. G. Mints, Phys. Rev. B **53**, 12311 (1996).
- ²⁰ E. H. Brandt and M. Indenbom, Phys. Rev. B **48**, 12893 (1993).

- ²¹ E. Zeldov, J. R. Clem, M. McElfresh, and M. Darwin, Phys. Rev. B **49**, 9802 (1994).
- ²² V. M. Vinokur, M. V. Feigel'man, and V. B. Geshkenbein, Phys. Rev. Lett. **67**, 915 (1991).
- ²³ E. H. Brandt, Phys. Rev. Lett. **76**, 4030 (1996).
- ²⁴ D. V. Denisov, A. L. Rakhmanov, D. V. Shantsev, Y. M. Galperin, and T. H. Johansen, Phys. Rev. B **73**, 014512 (2006).
- ²⁵ D. V. Denisov, D. V. Shantsev, Y. M. Galperin, E.-M. Choi, H.-S. Lee, S.-I. Lee, A. V. Bobyl, P. E. Goa, A. A. F. Olsen, and T. H. Johansen, Phys. Rev. Lett. **97**, 077002 (2006).
- ²⁶ I. S. Aranson, A. Gurevich, M. S. Welling, R. J. Wijngaarden, V. K. Vlasko-Vlasov, V. M. Vinokur, and U. Welp, Phys. Rev. Lett. **94**, 037002 (2005).
- ²⁷ R. G. Mints and E. H. Brandt, Phys. Rev. B **54**, 12421 (1996).
- ²⁸ A. Gurevich, Appl. Phys. Lett. **78**, 1891 (2001).
- ²⁹ J. I. Vestgård, D. V. Shantsev, Y. M. Galperin, and T. H. Johansen, Phys. Rev. B **84**, 054537 (2011).
- ³⁰ J. I. Vestgård, D. V. Shantsev, Y. M. Galperin, and T. H. Johansen, Sci. Rep. **2**, 886 (2012).
- ³¹ J. I. Vestgård, D. V. Shantsev, Y. M. Galperin, and T. H. Johansen, Supercond. Sci. Technol. **26**, 055012 (2013).
- ³² T. H. Johansen, M. Baziljevich, D. V. Shantsev, P. E. Goa, Y. M. Galperin, W. N. Kang, H. J. Kim, E. M. Choi, M.-S. Kim, and I. Lee, Europhys. Lett. **59**, 599 (2002).
- ³³ M. N. Wilson, *Superconducting Magnets* (Clarendon Press Oxford, 1983).
- ³⁴ M. Baziljevich, A. V. Bobyl, D. V. Shantsev, E. Altshuler, T. H. Johansen, and S. I. Lee, Physica C **369**, 93 (2002).
- ³⁵ C. Stahl, S. Treiber, G. Schütz, and J. Albrecht, Supercond. Sci. Technol. **26**, 015007 (2013).
- ³⁶ E.-M. Choi, H.-S. Lee, H.-J. Kim, S.-I. Lee, H.-J. Kim, and W. N. Kang, Appl. Phys. Lett. **84**, 82 (2004).
- ³⁷ E.-M. Choi, H.-S. Lee, H. J. Kim, B. Kang, S. Lee, Å. A. F. Olsen, D. V. Shantsev, and T. H. Johansen, Appl. Phys. Lett. **87**, 152501 (2005).
- ³⁸ J. Albrecht, A. T. Matveev, M. Djupmyr, G. Schütz, B. Stuhlhofer, and H. Habermeier, Appl. Phys. Lett. **87**, 182501 (2005).
- ³⁹ E.-M. Choi, V. V. Yurchenko, T. H. Johansen, H.-S. Lee, J. Y. Lee, W. N. Kang, and S.-I. Lee, Supercond. Sci. Technol. **22** (2009).
- ⁴⁰ S. Treiber and J. Albrecht, New Journal of Physics **12**, 093043 (2010).
- ⁴¹ F. Colauto, E. Choi, J. Y. Lee, S. I. Lee, E. J. Patiño, M. G. Blamire, T. H. Johansen, and W. A. Ortiz, Appl. Phys. Lett. **96**, 092512 (2010).
- ⁴² P. Mikheenko, A. J. Qviller, J. I. Vestgård, S. Chaudhuri, I. J. Maasilta, Y. M. Galperin, and T. H. Johansen, Appl. Phys. Lett. **102**, 022601 (2013).
- ⁴³ E. H. Brandt, Phys. Rev. B **52**, 15442 (1995).
- ⁴⁴ B. J. Roth, N. G. Sepulveda, and J. P. Wikswo, Jr., J. Appl. Phys. **65**, 361 (1989).
- ⁴⁵ U. Bolz, B. Biehler, D. Schmidt, B. Runge, and P. Leiderer, Europhys. Lett. **64**, 517 (2003).